Submitted on 24 September, 2007.

COMPTON SCATTERING

Dylan R. Nelson
Department of Physics, University of California, 366 LeConte Hall, Berkeley, CA 94720-7300: dnelson@berkeley.edu

Partner: Joey Cheung
Department of Physics, University of California, 366 LeConte Hall, Berkeley, CA 94720-7300: jpc168@berkeley.edu

ABSTRACT

We present the results of our investigation of the Compton effect, whereby high energy photons scatter off free electrons, depositing a fraction of their initial energy. The shortcomings of the classical Thompson scattering cross section are discussed, and the quantum mechanically correct Klein-Nishina model is presented. We use a Si(Li) semiconductor detector to measure the spectra of ^{55}Fe and ^{241}Am , characterizing its response and calibrating with known emission lines. We achieve a detector resolution corresponding to line FWHMs of 450 ± 6 eV and 3.7 ± 0.1 channels for the 59.54 keV line of ^{241}Am and the second peak of ^{55}Fe , respectively. Fitting Gaussian profiles then enables sufficient accuracy to measure emission line centers and widths.

Using this method, we explore the angular dependence of the Compton effect by taking integrations at seven different scattering angles. Our results are in general agreement with the K-N prediction, while an absolute comparison of cross section magnitudes will require much tighter constraints on the relevant errors. By fitting the energy shift as a function of angle we calculate the mass of the electron to be 480.9 ± 57.1 keV, in agreement with its accepted value. Finally, by observing a monoenergetic beam of 59.54 keV photons we attempt a measurement of the Compton continuum. Although we identify the backscatter peak at 48.85 keV and the Compton edge at 11.25 keV, experimental shortcomings prevent a quantitative comparison to the theoretical electron energy distribution.

Subject headings: Compton scattering; Compton effect; Atomic scattering; cross sections; X-ray scattering

1. INTRODUCTION

Compton scattering is the decrease in energy of an energetic photon (typically x-ray or γ-ray) scattered off of an electron. The total change in energy ΔE is called the Compton shift. This phenomenon provides support for the particle nature of light, as the decrease in energy cannot be explained by a purely wave formulation.

One of the first applications of the relativistically correct quantum theory of electrodynamics (QED) was the prediction by Klein and Nishina in 1929 of the angular dependence of the Compton effect. Their model gives the differential cross-section, and thereby the likelihood of interaction between an incoming particle and a target, as a function of scattering angle.

Our goal, in brief, is to scatter high-energy photons from an aluminum target at various scattering angles, and measure their final energies, enabling us to observe and analyze the effects of Compton scattering. In §2 we explore the necessary theoretical background, while §3 describes the experimental setup and observational procedures. We consider the angular dependence in §4.1, calculate the mass of the electron in §4.2, and measure the Compton "continuum" background in §4.3. A summary of pertinent results is given in §5.

2. THEORY

The energy shift of scattered electromagnetic radiation can be understood if we consider the incident light as photons striking electrons, and invoke an energy-momentum conversation argument. We assume the target electron to be at rest (or at least having $v \ll c$), a fairly good assumption in a conductor such as aluminum. Restricting the effect to two-dimensions, such that the initial and final momentum vectors all lie in the same plane, the difference between the final wavelength λ' and the initial wavelength λ is given by

$$\lambda' - \lambda = \frac{h}{m_e c^2} \left(1 - \cos\theta\right), \tag{1}$$

where θ is the photon scattering angle. Using the relation $\lambda\nu = c$, and well as a photon energy given by $E_\gamma = h\nu$, we can solve (1) for the scattered photon energy.

$$E' = \left(\frac{1 - \cos\theta}{m_e c^2} + \frac{1}{E}\right)^{-1} = \frac{E}{1 + (1 - \cos\theta)E/m_e c^2}. \tag{2}$$

The likelihood for an incoming particle to scatter with a given target is traditionally given by a cross-section, with units of area, corresponding to the effective size of the target as "seen" by the particle. In this case, the relevant quantity is the Thomson total cross-section (that is, integrated over all angles θ), which is given by

$$\sigma_{\mathrm{T}} = \frac{8\pi}{3} \left(\frac{e^2}{mc^2}\right)^2 \tag{3}$$

in cgs units. However, this purely classical result has several problems. It is frequency independent (a fact in disagreement with experiment), discards the role of electron recoil (significant due to the relatively small mass), and ignores both relativistic and quantum mechanical effects. The QM-correct derivation is given by the Klein-Nishina (K-N) differential cross section

$$\frac{d\sigma}{d\Omega} = \frac{r_o^2}{2}\frac{1+\cos^2\theta}{[1+\gamma(1-\cos\theta)]^2} \cdot \left[1+\frac{\gamma^2(1-\cos\theta)^2}{(1+\cos^2\theta)[1+\gamma(1-\cos\theta)]}\right], \quad (4)$$

where $r_o = e^2/m_e c^2$ is the classical electron radius, and $\gamma = h\nu/m_e c^2$. For the 59.54 keV line, $\gamma \simeq 0.11 \ll 1$, and so $\sigma_{\rm KN}/\sigma_{\rm T} \simeq 0.83$. We compare this theoretical prediction with our results in §4.1.

2.1. *Compton Continuum*

Klein and Nishina also predicted a Compton continuum which will arise from scattering within the detector itself. In §4.3 we consider this effect by analyzing the scattered electron energy distribution $(d\sigma/dq')$. If q' is the energy of the scattered electron, then by the chain rule

$$\left(\frac{d\sigma}{dq'}\right) = \left(\frac{d\sigma}{d\Omega}\right)\left(\frac{d\Omega}{dq'}\right) = \left(\frac{d\sigma}{d\Omega}\right)\left(\frac{dq'}{d\Omega}\right)^{-1} = \left(\frac{d\sigma}{d\Omega}\right)\left(\frac{dq'}{2\pi\sin\theta d\theta}\right)^{-1}. \quad (5)$$

Here we use the fact that the solid angle $d\Omega = \sin\theta d\theta d\phi = 2\pi\sin\theta d\theta$ due to azimuthal symmetry. From conservation of energy we have

$$h\nu + m_e c^2 = k' + q', \quad (6)$$

where from (1) the scattered photon energy k' is given by

$$k' = \frac{h\nu}{1+\frac{h\nu}{m_e c^2}(1-\cos\theta)}. \quad (7)$$

Substituting our expression from (7) into (6) we can solve for $q'(\theta)$, the scattered photon energy as a function of angle. Differentiating, we find that

$$\frac{dq'(\theta)}{d\theta} = \frac{k'^2\sin\theta}{m_e c^2}. \quad (8)$$

Finally, substituting (8) back into (5) we find that the scattered electron energy distribution is related to the scattered photon angular distribution by

$$\left(\frac{d\sigma}{dq'}\right) = \left(\frac{d\sigma}{d\Omega}\right)\left(\frac{2\pi m_e c^2}{k'^2}\right). \quad (9)$$

We compare this theoretical energy distribution with our observations by directly radiating the detector by unscattered γ-rays in §4.3.

3. MEASUREMENTS

3.1. *Apparatus*

Compton scattering is the scattering of electromagnetic radiation by free electrons. Without a feasible way to have a population of stationary, free electrons as a target, we use instead an aluminum arc, within which the electrons are decidedly bound to nuclei. However, in the energy range of our ^{241}Am source, the light quanta have individual energies generally exceeding the binding energy of the electrons, allowing us to treat them as free electrons.

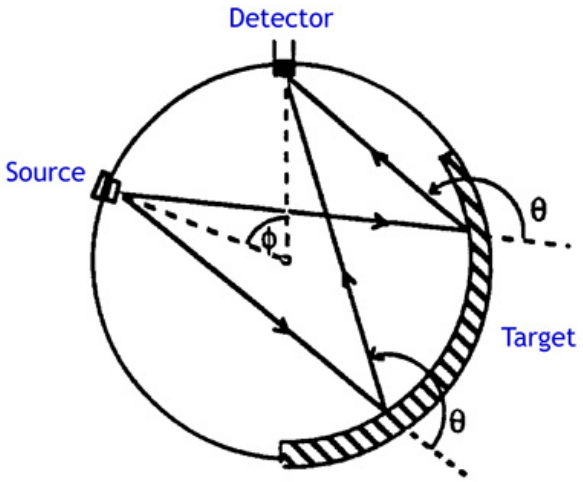

FIG. 1.— Diagram of the apparatus setup for measuring Compton scattering as a function of angle. θ represents the scattering angle, and ϕ the angle between the source and detector. The $^{\rm Al}$Big target (pictured) subtends 120° on a $R = 9.7$cm circle for an arc length of 20.3cm. The $^{\rm Al}$Small target subtends 60° with the same radius of curvature, for an arc length of 10.2cm, where both have a thickness of approximately one centimeter.

Our setup consists of the ^{241}Am source, aluminum target, and Si(Li) detector all placed at points on the same circle. The detector is fixed, and the source and target arranged to achieve a given scattering angle. From Figure (1), note that the angle ϕ between source and detector is related to the scattering angle θ by

$$\phi = 360° - 2\theta. \quad (10)$$

Furthermore, from geometry we see that two photons scattered from different points on the target and entering the detector are guaranteed to have the same angle θ. Consider two angles $\alpha_1 = 180° - \theta_1$ and $\alpha_2 = 180° - \theta_2$ both interior to the circle, formed between the two pairs of source-target and target-detector rays, as shown in Figure (1). Then, since α_1 and α_2 both correspond to the same arc on the circle, we know $\alpha_1 = \alpha_2$ and so $\theta_1 = \theta_2$. These details are used in §4.1 to convert from photon counts to effective cross section.

3.2. *Detector Characterization*

The detector we use is a lithium-drifted silicon, or Si(Li) semiconductor detector. At the energy ranges at use in this experiment ($E \leq 60$ keV), detections occur by means of the photoelectric effect. Other processes, such as pair production and bremstrahlung radiation only operate at higher initial photon energies. To minimize thermal noise at these energies, the detector is held at 77°K by liquid nitrogen in an attached dewar. Detection events result in small voltage pulses which are amplified and fed into a LeCroy 3001 Pulse Height Analyzer (PHA), which detects these pulses, determines their height, and forms

a histogram of counts over 1024 voltage channel bins. We operate the PHA primarily at the 10 mV/ch input resolution mode.

To characterize the system, we place a ^{55}Fe source next to the detector with an unobstructed path. Using an oscilloscope we calibrate the amplification electronics to output between zero and ten volts for the highest pulses, the appropriate input range for the PHA. ^{55}Fe has two emission peaks at 5.90 keV and 6.55 keV, shown in Figure (2) for the two different resolution settings available with the PHA.

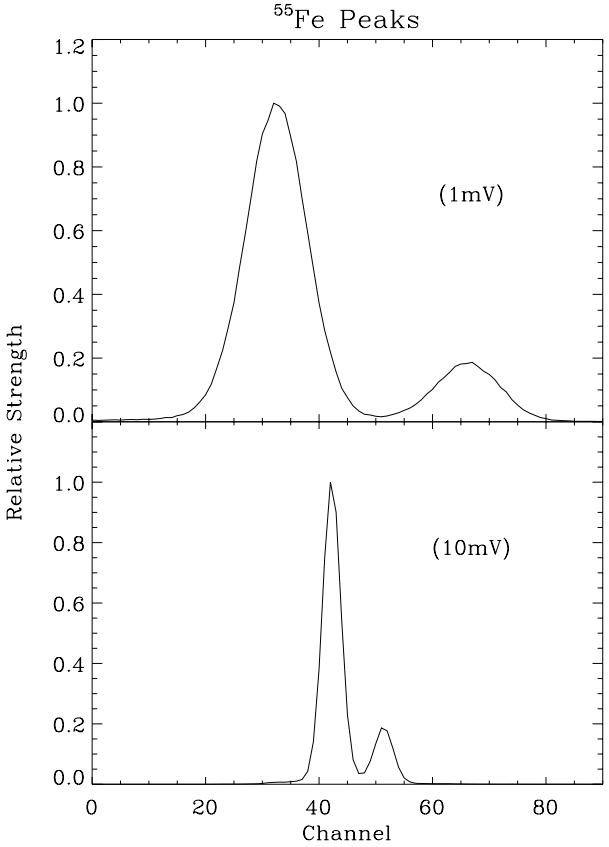

FIG. 2.— The two "twin peaks" of ^{55}Fe shown across 90 PHA channels at 1mV/ch resolution (upper panel) as well as 10mv/ch resolution (lower panel). The FWHMs of the two peaks at the higher resolution setting are 12.7 and 12.8 channels, and 3.7 and 3.6 channels at the lower resolution.

In both cases the two peaks are clearly resolved. With higher resolution the PHA is able to better separate the lines, as seen by the lower achieved minimum between the two. Ideally, in order to reduce errors during Gaussian fitting, we would like to use the higher resolution. However, the need to observe the 59.54 keV line for various scattering angles necessitates the lower resolution setting which allows us to record energies up to $\simeq$62 keV.

3.3. *Calibration*

In order to calibrate the response of the detector apparatus, we exploit the relationship between voltage pulse height output from the detector/amplifier system and the incident photon energy. That is, each channel of the PHA corresponds to a particular energy. The ^{241}Am source is placed along an unobstructed path to the detector, sufficiently far (15cm) to avoid the issue of high count rates and PHA "dead time." This is a consequence of the finite sampling time of the equipment, and that after registering a voltage pulse it must reset before a second pulse can be separately identified. Otherwise, a second pulse could be dropped or summed with the first. The sampled spectrum, as shown in Figure (3), reveals well-defined emission lines with relatively high SNR characteristics.

TABLE 1
^{241}Am Emission Lines

Energy	Relative Strength
13.5 keV	0.128
17.3 keV	0.224
20.9 keV	0.062
26.3 keV	0.028
59.54 keV	0.400

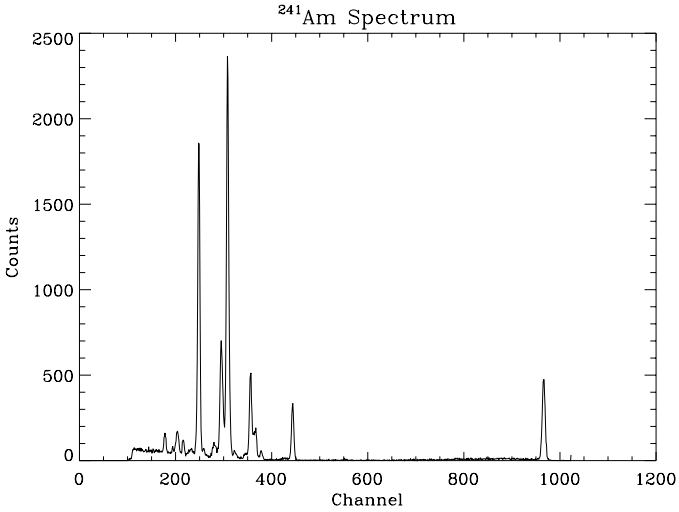

FIG. 3.— Unscattered ^{241}Am spectrum, taken with the source approximately 15cm from the detector, with a duration of 10 minutes. Here, total number of counts is plotted against uncalibrated channel number of the PHA. Each of the five primary emission lines is clearly visible, and background noise appears to have a negligible contribution.

Atomic spectroscopy has determined the emission lines of ^{241}Am to high precision, which are given in Table (1) along with their relative strengths.

Fitting one-dimensional Gaussian profiles to each of these emission lines using a simple χ^2 minimization allows us to calculate their centroids to sub-channel accuracy. An example of such a fit is shown in Figure (4).

Since radioactive decay is a Poisson process, we assign a statistical uncertainty to each point corresponding to a fractional error of $1/\sqrt{N}$. A 1σ uncertainty is then analytically calculated for each of the Gaussian fit parameters. Using the centroid plus uncertainty for each of the five emission lines, along with their corresponding energies from Table (1), we fit a linear relationship, shown in Figure (5).

We find an energy channel relation given by:

$$E = (0.0624 \pm 0.0013)\mathrm{CH} - (2.44 \pm 0.03)\ \mathrm{keV}. \quad (11)$$

This corresponds to an effective resolution of 62.4

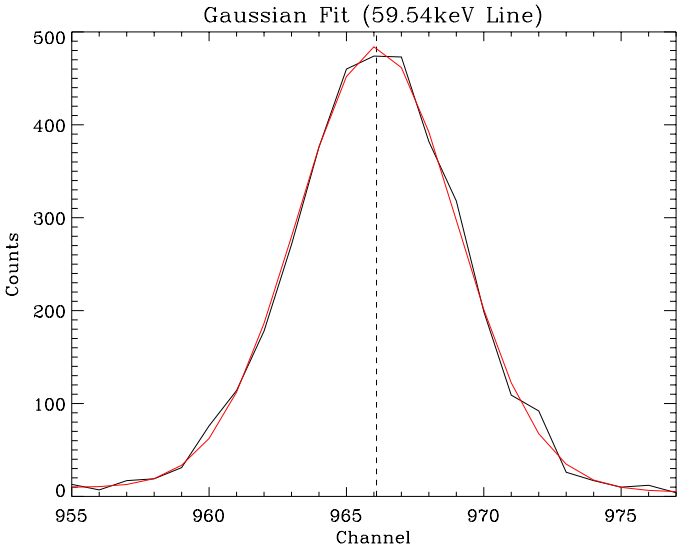

FIG. 4.— Sample Gaussian fit to one of the emission lines in the ^{241}Am calibration source spectrum, here the 59.54keV line. The data is plotted in counts per channel in black, where the overplotted red line represents the best fit Gaussian. The dashed line marks the center of the fit. We do automatic baseline subtraction by including constant, linear, and quadratic terms in the fitting process, for a total of six free parameters.

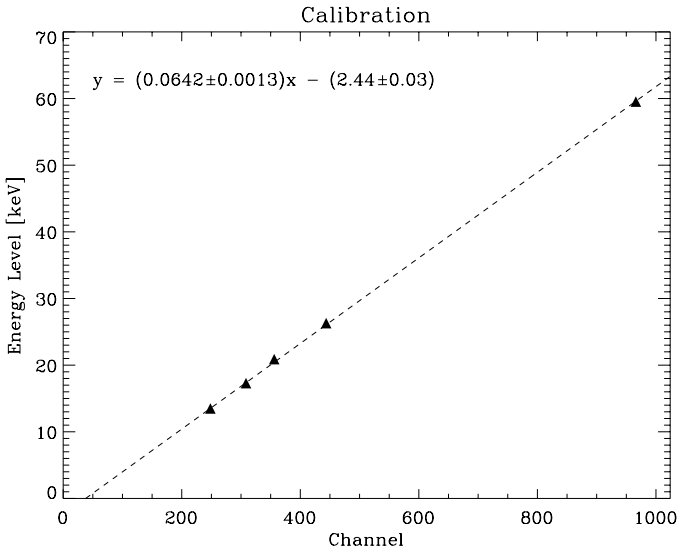

FIG. 5.— Linear fit between channel number and emission line energy enables us to calculate a calibration solution for each channel. The associated errors are given. Residuals between linear and higher order fits indicate that the detector response is well characterized by our linear assumption. $\chi^2 \simeq 0.01$ for this fit, indicating confidence above the 99% level.

eV/ch. Across 1024 channels this yields a detectable energy range of 0-61.5 keV. The intercept indicates that zero energy does not occur at channel number one, evidenced in all our spectra since the first ∼100 channels always show zero counts. For reference, the FWHM of the 59.54 keV calibration line is 7.2 ± 0.1 channels, or 450 ± 6 eV. For a lithium-drifted silicon detector at 77°K, we expect a FWHM of ≃3 keV for incident energies of ∼100 keV, and somewhat less at 59.54 keV.

3.4. *Observations*

Our primary observations are summarized in Table (2), where the duration, target used, source-target and target-detector distances are given for each scattering angle. For all angles we ensure that 100% of the target is illuminated by the source. Lead shields are used to prevent unscattered photons from entering the detector directly from the source.

TABLE 2
SUMMARY OF OBSERVATIONS

Angle[1] (°)	Duration (hr)	ST[2] (cm)	TD[3] (cm)	Target
165	70.34	18.9	19.8	^{Al}Big
130	22.25	18.4	15.0	^{Al}Big
105	23.00	16.9	15.0	^{Al}Big
90	23.92	14.5	14.5	^{Al}Big
80	27.50	13.2	18.7	^{Al}Big
60	21.50	11.0	8.9	^{Al}Small
45[a]	23.42	9.4	5.6	^{Al}Small

[1] Apparatus restrictions limited possible angles to between 40° and 170°.
[2] Source-target distance measured from the near face of the source to the near surface of the aluminum target.
[3] Target-detector distance measured from the target surface to the detector itself, 5mm behind the protective cap.
[a] Results from the $\theta = 45°$ run possibly contaminated by disruption of the setup partway through, and are a large point of error in future calculations.

For the verification of the Compton continuum emission in §4.3, we use a different setup. In a linear path outward from the detector we place a filter at 4.0 cm, two collimators at 7.5 cm and 10.7 cm, and the source at a distance of 15.5 cm. The filter contains Cu and Al sheets both of a thickness ≃0.003". Collimation is through two lead sheets with ≃1 mm apertures. All four elements are placed on the plane level with the detector. Effectively, we filter a collimated beam from the ^{241}Am source in order to obtain only the high-energy 59.54 keV peak at the detector. This monoenergetic beam scatters directly off electrons inside the detector, which we discuss further in §4.3.

Finally, we make a single 25.00 hour background observation with no sources present. The average activity per active channel per hour is only 0.171 ± 0.078 counts. With such low counting statistics, Poisson scatter is large, and we use a polynomial fit to effectively smooth the background spectrum before subtraction. This results in correction factors of ∼1% or less, but is included for completeness.

4. RESULTS AND DISCUSSION

4.1. *Angular Dependence*

Following the procedure described in §3 we measure the ^{241}Am spectrum as a function of scattering angle. One example is given in Figure (6), where we observe, as in the spectra for each other scattering angle, a prominent *unshifted* peak corresponding to 59.54 keV.

This unshifted peak is due to scattering off electrons that remain bound in the target atoms. From (2) we can see that when the recoil momentum is of the entire atom, the Compton energy shift is of order 1 eV, an undetectable effect given our experimental precision.

Using an identical Gaussian fitting procedure as that described in Figure (4), the *shifted* 59.54 keV line center was determined for each of the scattering angles observed. Using our calibration from (11), the centroids

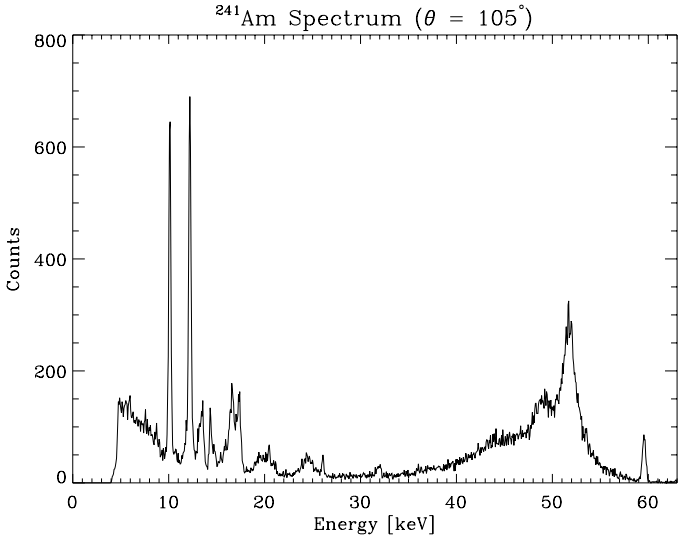

FIG. 6.— Example of a scattered ^{241}Am spectrum, taken at $\theta = 105°$ against the large aluminum target. Here, total number of counts is plotted against calibrated energy in keV. Total exposure time for this angle was 23.00 hours. The unshifted peak is evident at 59.54 keV, as well as the shifted peak at ∼52 keV.

were converted to energies.

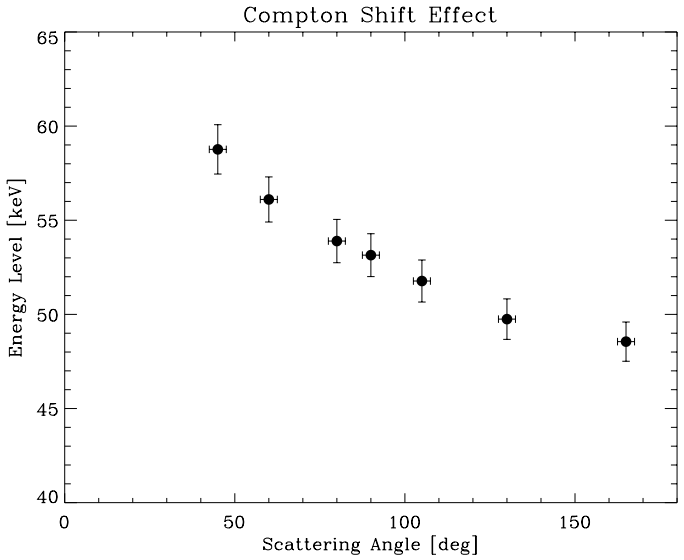

FIG. 7.— Scattered photon energy as a function of seven different scattering angles. We observe a downward though non-linear trend of energy with increasing angle, as expected from (2). An instrumental uncertainty in the angle of ±2.5° is estimated from precision limits in the experimental setup.

In order to compare our observed angular dependency with the Klein-Nishina prediction of (4) we need to first convert from count numbers to differential cross section. We integrate over the Gaussian fit to the 59.54 keV photopeak for each angle to obtain the total "yield" of the line. We call this value N_s the number of scattered photons *detected*. If N_i is the number of photons incident on the target, the differential cross section is given by

$$\frac{d\sigma}{d\Omega} = \frac{N_s/\Delta t}{N_i/\Delta t}\frac{1}{(d\Omega)_D N_e f_D}, \tag{12}$$

Where $(d\Omega)_D$ is the solid angle subtended by the detector, N_e is the total number of electrons in the target, and f_D is the detector efficiency. Divisions by Δt represent total counts normalized per unit time. The depth of the detector and effects of the Beryllium window are included in the f_D factor, such that N_s/f_D represents the predicted total number of scattered photons from the target into the solid angle $(d\Omega)_D$. The solid angle can be calculated as

$$(d\Omega)_D = \frac{A_D}{4\pi r_{\rm TD}^2} = \frac{\pi r_D^2}{4\pi r_{\rm TD}^2}, \tag{13}$$

where A_D is the projected detector area, which we take to be face-on and circular, and $r_{\rm TD}$ is the target-detector distance. In order to calculate N_i, effectively the incident flux at the target, we need the activity of the ^{241}Am source A given in Curies (Ci), where

$$1 \text{ Ci} = 3.7 \times 10^{10} \text{ disintegrations per second (dps)}.$$

If t is the time since the source calibration A_o was measured, and τ_m is the mean-life of the source, related to the half-life τ_h by $\tau_m = \tau_h/\ln(2)$, the current activity A is

$$A = A_o e^{-t/\tau_m}. \tag{14}$$

Finally, assuming that the source radiates isotropically, the total number of incident photons at some target a distance $r_{\rm ST}$ from the source is given by

$$N_i = \frac{F_D}{4\pi r_{\rm ST}^2} = \frac{A \cdot B_F \cdot B_R \cdot \Delta t}{4\pi r_{\rm ST}^2} \tag{15}$$

where F_D is the detector flux, given as the product of the activity A, elapsed time Δt, the branching fraction B_F for the mode of decay, and the branching ratio B_R of the particular photon energy. For the 59.54 keV line of ^{241}Am , $B_F = 0.94$ and $B_R = 0.36$. N_i will have units of photons/cm^2·s. We note that both the solid angle of (13) and the incident flux of (15) are variable due to changing $r_{\rm TD}$ and $r_{\rm ST}$ with angle.

The last unknown needed to calculate the differential cross section (12) is N_e, the number of electrons in the target, and thus the number of scattering centers presented to the incident photon beam. If N_A is Avogadro's number, Z the atomic number and A the atomic weight of the target, and ρ the mass density of the target, then

$$N_e = V \cdot \rho \cdot \frac{N_A \cdot Z}{A} = \alpha\,(2\pi R)\,h\ell_{\rm bt} \cdot \rho \cdot \frac{N_A \cdot Z}{A}, \tag{16}$$

where for the volume V of the target we take the arc circumference times a filling factor α by its height h and depth $\ell_{\rm bt}$ of interaction between beam and target. For $^{\rm Al}$Big $\alpha = 1/3$, and for $^{\rm Al}$Small $\alpha = 1/6$. For the aluminum target, $Z = 13$, $A = 27$, and $\rho = 2.7$ g/cm^3.

The total yield for each scattering angle, along with other quantities of interest, are given in Table (3), where N_i and N_s are both normalized to events per hour. The differential cross section is then calculated, and compared with the theoretical Klein-Nishina prediction for angles between 0° and 180° in Figure (8).

Our results support the general angular dependence of the scattering cross section. However, the errors involved in this calculation are significant. In summing over the

TABLE 3

Angle (°)	N_i (10^6 γ/cm^2·t)	N_s (γ/t)	$(d\Omega)_D$ (10^{-5} sr)	χ^2
165	1.185	852	6.50	1.71
130	1.249	630	6.50	1.72
105	1.473	431	5.10	1.31
90	2.121	549	4.11	1.46
80	2.376	926	4.82	1.57
60	3.373	895	6.50	1.40
45	4.460	1930	6.50	1.67

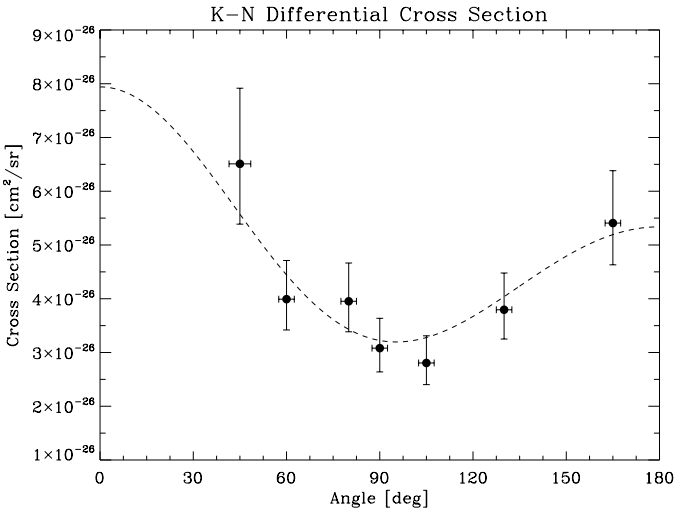

FIG. 8.— Differential cross section in units of cm^2/sr as a function of scattering angle. The theoretical Klein-Nishina prediction of (4) is shown as a dotted line, and the calculated cross sections for each of our seven scattering angles are shown as filled circles with appropriate uncertainties indicated.

Gaussian profile of the photopeak we incorporate the 1σ uncertainties in peak position and width. Still, asymmetric line profiles are present, e.g., in the 45° spectrum, which invalidates the Gaussian shape assumption. Likely, a more sophisticated method for determining the effective line widths is called for.

We include the reduced χ^2 goodness-of-fit statistics in Table (3), which quantify the degree to which each 59.54 keV photopeak assumes the theoretical profile. For six degrees of freedom in our Gaussian fits, these χ^2 values indicates confidence at the 90% level and above. However, these fits may not necessarily include the total number of events related to a given emission line.

In (12) the calculation of $(d\Omega)_D$, N_i, and N_e all depend on basic physical length measurements made with a ruler. Furthermore, the cross section dependence on these measurements is relatively high (e.g. $\sigma \propto r^{-2}$). Finally, uncertainty in the general setup of the apparatus leads to a small though noticeable error in scattering angle.

With appropriate caution, we conclude that our data agrees with the Klein-Nishina model with regards to scattering angle, though it lacks the experimental accuracy to verify the magnitude of the cross section at any one angle.

4.2. *Electron Mass*

We perform a calculation less sensitive to the errors involved in order to make a highly accurate measurements of the mass of the electron. Letting $\Delta\mathrm{E}^{-1} = (1/E' - 1/E)$, a linear relation between this inverse energy difference and $(1 - \cos\theta)$ follows from (1) re-expressed in terms of energy:

$$\Delta E^{-1} \equiv \frac{1}{E'} - \frac{1}{E} = \frac{1}{m_e c^2}\,(1 - \cos\theta)\,. \qquad (17)$$

Our seven data points and best-fit are shown in Figure (9).

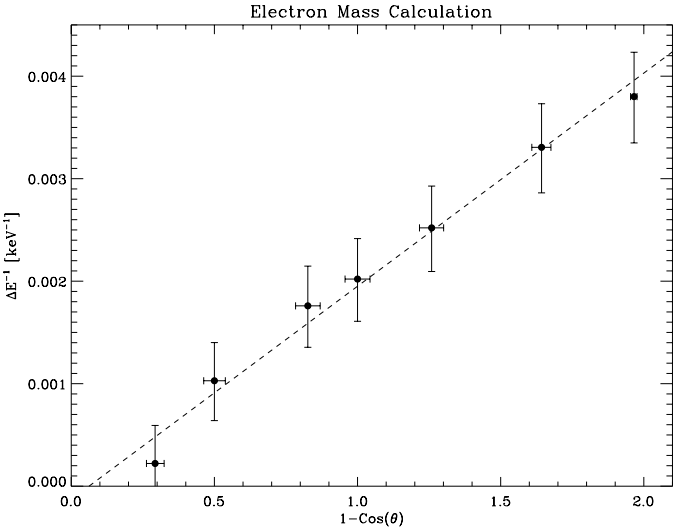

FIG. 9.— Inverse energy shift $\Delta\mathrm{E}^{-1}$ as a function of $(1 - \cos\theta)$, where θ is the scattering angle. Errors on both parameters are indicated, and a best-fit linear solution is shown as the dashed line. This fit has a slope of 0.00208 and a y-intercept of 0.00013, where we expect a zero y-intercept, and deviation from zero indicates an error factor of order $1/E$.

By inverting the slope, we calculate the mass of the electron to be 480.9 ± 57.1 keV, where the accepted value is 511.0 keV, well within our uncertainty. Our rather large error ($\simeq$15%) was calculated by (1) attributing $1/\sqrt{N}$ statistical uncertainty to each PHA bin count; (2) propagating the error on the calibration solution to the energy conversion for each Gaussian centroid; (3) combining the uncertainty in the 59.54 keV Gaussian fit with that from calibration; and (4) propagating that error to $\Delta\mathrm{E}^{-1}$, together with uncertainty in $(1 - \cos\theta)$ as described in Figure (7), in order to calculate a weighted best-fit line to the points in Figure (9). We feel it represents a robust estimate of the 1σ uncertainty involved in this process.

In this calculation we assumed a monoenergetic beam of incident photons, which is untrue. While in §4.3 we filter the ^{241}Am source in order to obtain only a single line, here we have multiple emission peaks possibly leading to contamination of our measurements. Furthermore, the geometry of the target is such that a range of effective scattering angles about the desired angle is unavoidably obtained. This leads to a broadening of the 59.54 keV peak, and so is unlikely to significantly affect the centroid measurements used in this section to estimate the mass of the electron.

4.3. *Compton Continuum*

Following the procedure described in §3.4, we exposure the detector to an unscattered beam of monoenergetic

59.54 keV photons. Compton scattering off electrons inside the detector should then take place. In this scenario, the particle that gives rise to the Compton distribution is the energized electron after the collision. From (1) we know the maximum energy transfer occurs in the case of back-scattering ($\theta = 180°$), in which case the maximum energy is

$$E_{\rm CE} = \frac{E_\gamma}{1 + (m_e c^2/2E_\gamma)}, \tag{18}$$

where E_γ is the energy of the incident photon. For the 59.54 keV line, this yields a final energy of 48.29 keV, a Compton shift of ΔE = 11.25 keV. This forms the end of the Compton distribution, and is known as the *Compton edge*. Since the final electron energy is a function of scattering angle, we expect to observe a Compton continuum, as predicted by Klein and Nishina. For low energy shifts, the theoretical cross section is given in Figure (10).

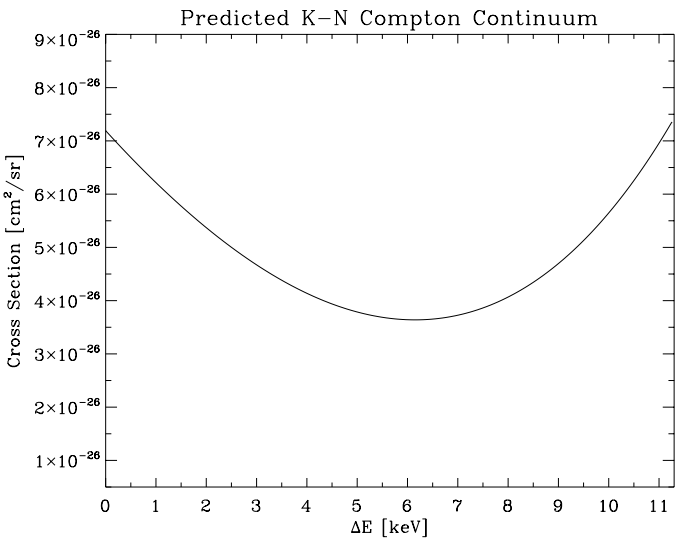

FIG. 10.— The predicted differential cross section in cm^2/sr as a function of scattering angle off electrons inside the detector. The shape is roughly parabolic with total change in cross section of a factor of ∼2 over the energy range.

Our continuum observation had a total duration of 69.00 hours. Using calibration as before, our integrated spectrum is shown in Figure (11), with raw channel number converted to energy, and features of interest marked.

Examining Figure (11), the original unshifted emission at $E_o = 59.54$ keV is still evident, as expected. The large backscatter peak at $(E_o - \Delta E) = 48.29$ keV shadows the photopeak in the theoretical energy position, where the broadness arises from the 180° scattering angle being only approximately fulfilled. The spectrum also measures the electron energy distribution, where by conservation of momentum $\Delta E_e = -\Delta E_\gamma$. The maximum electron energy of 11.25 keV, representing the Compton edge, which is indicated by the dashed line at the lowest energy. To the left (i.e., towards lower energies) of this point we expect Compton continuum emission for all scattering angles between zero and 180°.

Due to failure in the apparatus, a large number of energy channels (∼100) are dead, or otherwise always report zero counts. Comparing qualitatively with Figure (10), our results are perhaps consistent in the narrow

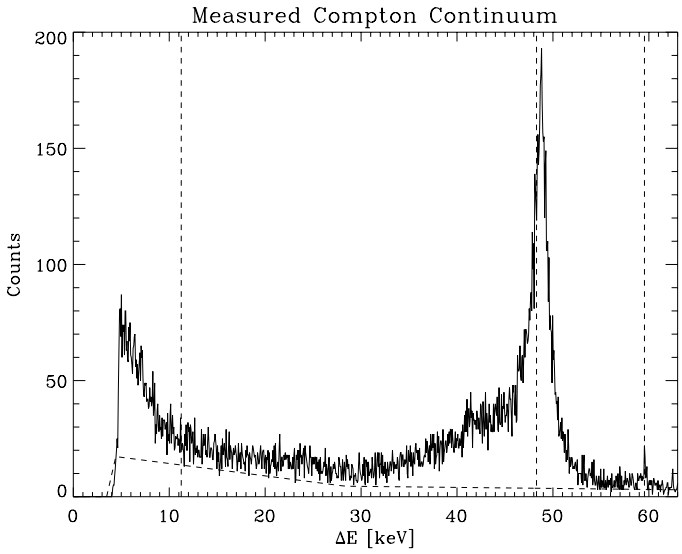

FIG. 11.— Number of counts plotted against energy bin on the PHA for our Compton continuum observation. Integrated for a total of 69 hours, the original peak is still visible at 59.54 keV. The expected locations of the Compton edge and backscatter peak are indicated with vertical dashed lines. The horizontal dashed line represents the background level, appropriately scaled.

energy range 5-7 keV. From 0-5 keV we are unable to make a comparison. Between 7 keV and the Compton edge at 11.25 keV our observed electron energy distribution trends downward, while the prediction is an upward trend or at least a plateau. The reason for this is unclear. It may be a detector sensitivity issue, or perhaps a nonlinearity at low energies leading to incorrect calibration. Other scattering processes are likely also contributing to the observed spectrum. Multiple Compton scatterings inside the detector are certain, where the last collision may be either a Compton or photoelectric event.

At other energy levels we are essentially observing background counts. These may arise from cosmic rays, thermal excitation, or other nearby sources. For comparison, our background fit is plotted as the horizontal dotted line under the spectrum. To quantitatively compare the observed Compton continuum with the Klein-Nishina prediction a longer integration and more careful background subtraction are called for. Alternatively, different source / detector combinations are more suited to observing this effect (e.g., ^{137}Cs and a NaI scintillator detector), especially at initial γ-ray energies greater than ∼250 keV where the Compton edge and backscatter edge change positions with respect to the photopeak.

5. CONCLUSION

The scattering of individual quanta of electromagnetic energy from electrons is a phenomenon that can be understand only in the context of quantum mechanics. We first explored the classical theory of Compton scattering, and then introduced the model of Klein and Nishina, which includes the angular dependence of the scattering angle. We characterized the response of our Si(Li) detector and calibrated it by using known emission lines from ^{55}Fe and ^{241}Am sources.

By collecting spectra from ^{241}Am at seven different scattering angles, we were able to calculate the differential cross section and compare with theory. We found a general agreement between our angular dependence and

that predicted by the Klein-Nishina model, while an absolute comparison of the cross section magnitudes would require much better constraints on the errors involved. By measuring the energy shift of the 59.54 keV emission line of ^{241}Am we were also able to estimate the mass of the electron as 480.9 ± 57.1 keV, in agreement with its accepted value.

Finally, by illuminating the detector with a filtered beam containing only the emission line at 59.54 keV, we hoped to measure the Compton continuum arising from photons scattering off electrons within the detector itself. Although we identified characteristic components of the resulting energy distribution, our results did not exhibit strong evidence of the low energy Compton continuum itself. However, the general approach of this experiment was found to be sound, and improvements in measurement accuracy and error minimization would lead to even more conclusive results.

Acknowledgements. The author would like to thank his partner, Joey Cheung, our GSI Ben MacBride, lab director Don Orlando, and professors K. Luk and D. Budker for their continual assistance.

REFERENCES

Giauque, R.D. et al., *Trace Element Analysis with Semiconductor Detector X-Ray Spectrometers*. LBL-647, Lawrence Berkeley Lab, p1-53.

Gibson, W. M., Miller, G. L., & Donovan, P.F., *Semiconductor Particle Spectrometers*. Alpha-,Beta-, and Gamma-Ray Spectroscopy, Siegbahn, K.: vol. 1, Ch. VIB, 1965, p345-378.

Goulding, F. S., *Semiconductor Detectors for Nuclear Spectrometry*. UCRL-16231, Lawrence Radiation Lab, p1-169.

Goulding, F.S., *A Survey of the Applications and Limitations of Various Types of Detectors in Radiation Energy Measurement*. UCRL-11302, Lawrence Radiation Lab, p1-31.

Knoll, G. F., *Radiation Detection and Measurement*. John Wiley & Sons, 1st ed., 1979.

Landis, D. A. et al, *Pulsed Opto Feedback X-Ray Spectrometer System*. LBL-540, Lawrence Berkeley Lab, 1972, p1-49.

Michael, F. L., Annunziata, M. M., & El Baradei, W. B., *Handbook of Radioactivity Analysis*. Elsevier Publishing, 2003.

Melissinos, A. C., & Napolitano, J., *Experiments in Modern Physics*. Academic Press, 2nd ed., 2003.

Nishina, T. & Klein, O., Z Physik, v52 11-12, 1929, p853-868.

Taylor, J. R., *An Introduction to Error Analysis*. University Science Books, 2nd ed., 1997.